ISSN (Print) 1226-1750
ISSN (Online) 2233-6656
Journal of Magnetics 21(1), 94-101 (2016) http://dx.doi.org/10.4283/JMAG.2016.21.1.094

Analysis of an Interior Permanent-Magnet Machines with an Axial Overhang Structure based on Lumped Magnetic Circuit Model

Jangho Seo[1]* and Jung-Moo Seo[2]

[1]*School of Automotive Engineering, Kyungpook National University, Sangju 37224, Korea*
[2]*Korea Electronics Technology Institute, Gyeonggi 13509, Korea*

(Received 18 November 2015, Received in final form 11 February 2016, Accepted 15 February 2016)

This paper shows a new magnetic field analysis of an interior permanent magnet (IPM) machines with an axial overhang structure wherein the rotor axial length exceeds that of the stator. The rotor overhang used to increase torque density of the radial flux machine is difficult to analyze because of extra consideration of axial direction, and thus it is general for machine designer to take 3-D finite element analysis (FEA) capable of considering both radial and axial complicated geometry in the machine. However, it requires too much computing time for preliminary design especially for optimization process. Therefore, in this paper a 2-D analytic method using a lumped magnetic circuit model (LMCM) is proposed to overcome the problem. For the analysis of overhang effect, the magnetic circuit is separated and solved from overhang and non-overhang regions respectively. For the validation of proposed concept, 3-D finite element analysis (FEA) is performed. From the analysis results, it is shown that our new proposed method presents good performance in terms of calculating electromotive force (EMF) and torque within a short time. Therefore, the proposed model can be useful in design of IPM with an overhang structure.

Keywords : FEA, overhang structure, interior permanent magnet (IPM) machines

1. Introduction

Recent developments in magnetic materials and the availability of modern power electronic, permanent magnet (PM) machines are becoming attractive. Among various type of PM machines, radial flux interior permanent magnet (IPM) machines has received more and more attention because it has additional component called reluctance torque and it has easier implementation of field weakening control.

The rotor overhang which is longer than stator core is generally used for simply enhancing torque density without increasing input current or overall stator's size [1-5]. In the design of IPM, 2-D FEA is widely used because it can consider complicated geometry and nonlinear magnetic B-H curve effectively. In case of IPM with overhang structure, the use of 3-D FEA is necessary to ensure analysis accuracy. However, the data storage space and calculating time for a 3-D FEA may be prohibitive especially in repetitive preliminary design process.

Several researches for the overhang effect have been introduced with the aim of reducing the computing time in 3-D FEA [1-5]. However, most of them is about surface permanent magnet (SPM) machines [3-5]. Kim *et al.* [1, 2] calculated overhang effect of IPM by introducing a design of experiment technique from 3-D FEA and employed 2-D FEA with revised B_r. Nevertheless, it still needs the time-consuming 3-D FEA. Li Zhu *et al.* introduced a effective analytical model for open-circuit air-gap field in IPM. However, it could not take into account both the overhang effect and torque associated with current angle.

Therefore, in this paper, to deal with these problems of conventional methods, a new 2-D analytical model based on a lumped circuit model (LMCM) is proposed for calculating the overhang effect in both in open-circuit and load condition. For the analysis of overhang structure, a magnetic circuit is separated and solved from non-overhang and overhang regions respectively. For validation of the proposed concept, air-gap flux density, back-electromotive force (EMF), and torque concerned with current angle is estimated by proposed method within a short

*Corresponding author: Tel: +82-54-530-1408
Fax: +82-54-530-1409, e-mail: j.seo@knu.ac.kr

time. The calculated results are compared with 3-D FEA.

2. General Analysis Models of IPM

2.1. Calculation of Air-Gap Magnetic Flux density by LMCM

The IPM machine with concentrated winding of eight poles and twelve slots is selected as an analysis model for verification of our proposed method. The configuration and specification of the model are shown in Fig. 1 and Table 1.

Magnetic flux lines by PM are presented in Fig. 1 which is used for calculating open-circuit field assuming smooth stator.

The influence of load and stator slotting will be account in the next section in detail. P is the number of magnet poles and a_P is the pole-arc to pole-pitch ratio. w_M and h_M are magnet width and magnet height respectively.

Fig. 2(a) shows the LMCM of IPM associated with flux distribution and leakage flux as presented in Fig. 1. ϕ_g is the air-gap fluxes excited by PM over one magnet pole and corresponding reluctance is R_g. ϕ_r and ϕ_{mo} are the flux

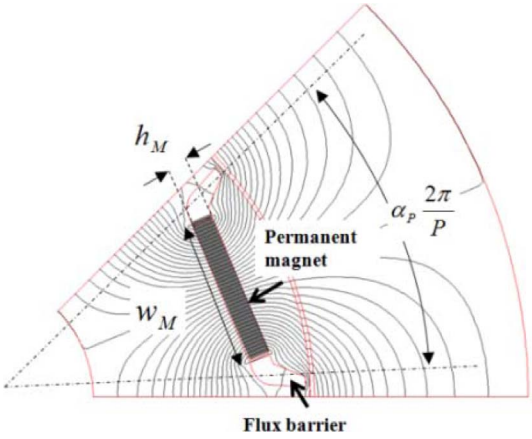

Fig. 1. (Color online) Cross section of analysis model under open-circuit magnetic field.

Table 1. Specifications of analysis model.

Parameters	Value	Unit
Pole/slot number	8/12	–
Pole-arc to pole-pitch ratio	0.88	–
Rated current	30	A
Air gap length	0.8	[mm]
Out diameter of stator core	230	[mm]
Out diameter of rotor core	140	[mm]
Axial length of the stator core	100	[mm]
Axial length of the rotor core	120	[mm]
Residual flux density of PM	1.2	[T]

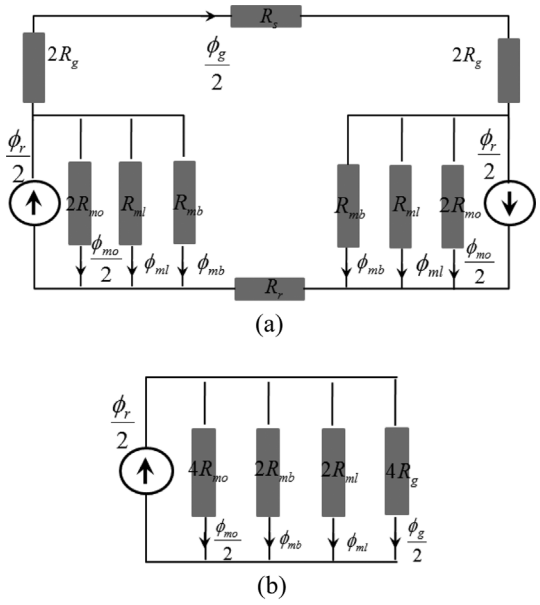

Fig. 2. LMCM of IPM machine under open-circuit condition. (a) Lumped magnetic circuit for Fig. 1. (b) A simplified form of Fig. 2(a)

source and the leakage flux of PM, the corresponding leakage flux reluctances being R_{mo}. ϕ_{mb} is the leakage flux through the bridge and the corresponding reluctance is R_{mb}. ϕ_{ml} is the magnet end-leakage fluxes, and the corresponding reluctances is R_{ml}. R_r and R_s are the reluctances of the rotor yoke and the stator yoke. In general, R_r and R_s may be neglected in comparison with R_g because there is no significant magnetic saturation in the yoke.

Due to symmetry, Fig. 2(a) can be simplified into Fig. 2(b). With reference to Fig. 1, the following expression can be obtained.

$$\phi_r = B_r A_m = B_r w_M L_{stk} \tag{1}$$

$$R_g = g / (\mu_0 A_g) \tag{2}$$

$$R_{mo} = \frac{h_M}{\mu_0 \mu_r A_m} \tag{3}$$

$$R_{ml} = \frac{h_M}{\mu_0 L_{stk} (h_1 + h_2)/2} \tag{4}$$

$$A_g = \alpha_p \frac{2\pi r}{P} L_{stk}$$
$$r = \begin{cases} \mathrm{R_i} - \mathrm{g}/2 & \text{radius for center of air - gap} \\ \mathrm{R_i} & \text{radius for stator bore} \end{cases} \tag{5}$$

where μ_0 is the permeability of air, μ_r is the magnet relative permeability, B_r is the residual flux density of PM, L_{stk} is the stack length of stator core, g is the air-gap

length, and R_i is the stator bore radius. h_1 and h_2 are the length of barrier. The leakage flux through the bridge can be approximated as

$$\phi_{mb} \approx B_{sat} A_b . \tag{6}$$

where $A_b = bL_{st}$ denotes the cross-sectional area of the bridge, b is the bridge width, B_{sat} is the saturation level on the B-H curve of magnetic steel. In general, the bridge is designed to be highly saturated like as 2.0 T [7-9].

Based on Fig. 2(b), air-gap flux can be expressed by

$$\varphi_g = \frac{(\varphi_r - 2\varphi_{mb})R_g}{1/R_{mo} + 2/R_{ml} + 1/R_g} . \tag{7}$$

Therefore, the air-gap flux density excited by PM is

$$B_g = \frac{\phi_g}{A_g} . \tag{8}$$

By substituting the calculated reluctance of (2)-(4) into (7) and (8), the air-gap magnetic flux ϕ_g and flux density B_g are determined.

From Fig. 1, indicating flux distribution through α_P and (8), the air-gap flux density waveform can be easily constructed as

$$B_{open} = B_g(\alpha) . \tag{9}$$

where a is the angular position referred to the stator.

2.2. Slot Opening Effect on Air-Gap Flux Density

There are several analytical models of permeance. One of them, relative permeance (RP) which is derived from the conformal mapping is adopted for considering stator's slotting effect [12-14]. The RP can be expressed as Fourier series.

$$\lambda(\alpha) = \sum_{m=0} \lambda_m \cos mQ_s(\alpha + \alpha_{sa}) \tag{10}$$

where Q_s is number of stator slots, λ_m is harmonic magnitude of the air-gap RP, and

$$\alpha_{sa} = \begin{cases} 0 & \text{coil span odd number of slots} \\ \pi / Q_s & \text{coil span even number of slots} \end{cases} \tag{11}$$

Different from the conventional slot-opening effect on SPM machines, there is an additional enhancement of air gap flux density due to magnet flux path distortion in iron core [6]. This additional increasing effect can be easily considered by using effective coefficient k_{eff} [6]. Thus, the open-circuit flux density distribution at the stator bore of slotted motor is given by [6]

$$B_{slotted}(\alpha) = B_g(\alpha) \cdot k_{eff} \times \lambda(\alpha) . \tag{12}$$

3. Proposed Method

3.1. Back-EMF Calculation considering Slotting Effect

Exact calculation of back-EMF is essential for the correct prediction of motor performance. For example, the peak value of back-EMF should be lower than DC link voltage connected to the motor under fault condition at maximum speed. Furthermore, the fundamental amplitude of the back-EMF determines the magnet torque of motor directly.

Conventional approaches for EMF is based on teeth flux by calculating average flux density according to the rotor position or average value of relative permeance [3-11]. However, these methods cannot account for the peak value of the EMF. Although the analytical models of subdomain and complex permeance can predict the EMF with very high accuracy, these models require both radial and circumferential flux density. Thus, a new EMF equation with only radial flux is derived in this section.

By approximating the coil as a current sheet over the slot opening, the flux linking a stator coil is calculated based on the radial flux density distribution along the stator bore:

$$\psi = \int_{-\alpha_y/2}^{\alpha_y/2} B_{slotted}(\alpha) R_i L_{st} d\alpha \tag{13}$$

where a_y is coil pitch , i.e. coil span, in mech. radian.

For integration of (13), (12) should be expressed by analytical equation.

$$B_{slotted}(\alpha) = \sum_{n=1,3,5} B_n \cos np(\alpha - \omega_r t) \times \lambda(\alpha) \tag{14}$$

where B_n is nth order harmonics of radial air-gap flux density, p is the number of pole pair, and ω_r is the mechanical rotor speed.

Using (10), (13) and (14), the flux linkage of a coil can be expressed by

$$\begin{aligned} \psi = & \sum_m \sum_n \lambda_m B_n R_i L_{st} \cos(mQ_s \alpha_{sa}) \cos(np\omega_r t) \\ & \times \frac{1}{mQ_s \pm np} \sin\left[\frac{\alpha_y}{2} (mQ_s \pm np) \right] \end{aligned} \tag{15}$$

Therefore the Back-EMF induced in each turn of coil is

$$\begin{aligned} e_{coil} = & \frac{d\psi}{dt} \\ = & -\sum_m \sum_n \lambda_m B_n R_i L_{st} \cos(mQ_s \alpha_{sa}) \sin(np\omega_r t) \\ & \times (np\omega_r) \times \frac{1}{mQ_s \pm np} \sin\left[\frac{\alpha_y}{2} (mQ_s \pm np) \right] \end{aligned} . \tag{16}$$

Hence for a distributed multi-pole winding, the induced

Back-EMF per phase is obtained as

$$e_{phase} = -N_{ph}\sum_{m}\sum_{n}\lambda_m K_{dn} B_n R_l L_{st}\cos(mQ_s\alpha_{sa})\sin(np\omega_r t) \times (np\omega_r)\times\frac{1}{mQ_s \pm np}\sin\left[\frac{\alpha_y}{2}(mQ_s \pm np)\right] \quad . \quad (17)$$

where N_{ph} is number of turns per phase in series and K_{dn} is nth order harmonics of distribution factor. Finally, the back-EMF taking into account slotting effect can be estimated using only radial component of flux density obtained from (9).

3.2. Calculation of Permeance for Overhang Effect

In order to consider the effect of overhang structure on the performance, the analysis model is separated into two parts, as shown in Fig. 3. Part I and Part II denote the nonoverhang and overhang region respectively. In the analysis, it is assumed that the individual region does not affect each other.

The magnet flux is selected as a key parameter capable of expressing the overhang effect because it is clear to quantify the effect whereas the flux density is ambiguous to be determined accurately.

The total magnetic flux is estimated by adding up the fluxes of Part I and II as

$$\phi_{g,total} = \phi_{g,PartI} + \phi_{g,PartII} \times 2 \, . \quad (18)$$

ϕ_{g_PartI} is directly obtained by (7). It is necessary to model a permeance representing the flux flowing into the stator core to determine ϕ_{g_PartII}. Figure 4 shows a vector plot of magnetic flux density with a shape of circular in Part II. Based on Fig. 4, a simplified linkage flux pattern can be drawn as shown in Fig. 5.

With overhang length, L_{OH} and the linkage flux pattern in Fig. 5, the air-gap permeance of Part II can be expressed by

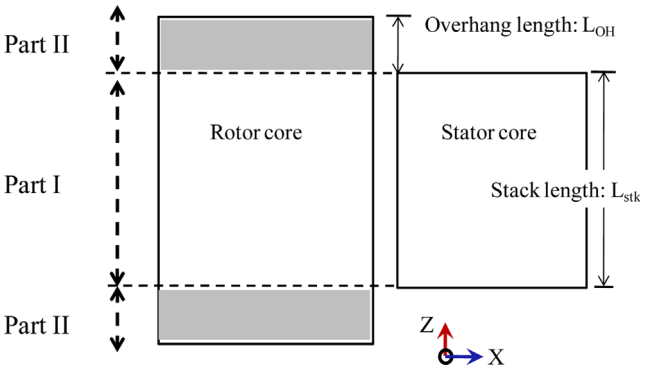

Fig. 3. (Color online) Separated regions for overhang effect. Part I is for non-overhang and Part II is for overhang region.

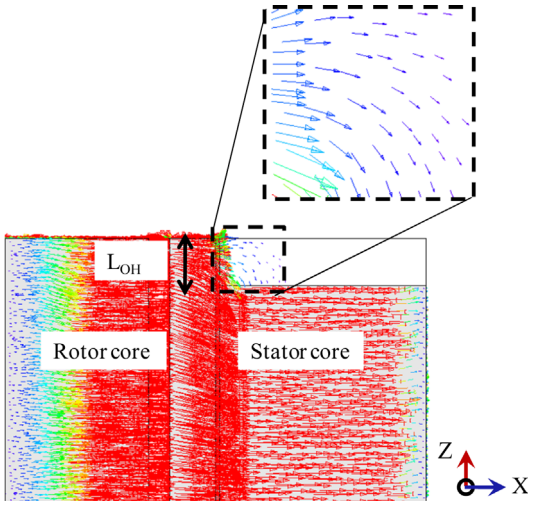

Fig. 4. (Color online) Side view: Vector plot of magnetic flux density using 3-D FEA.

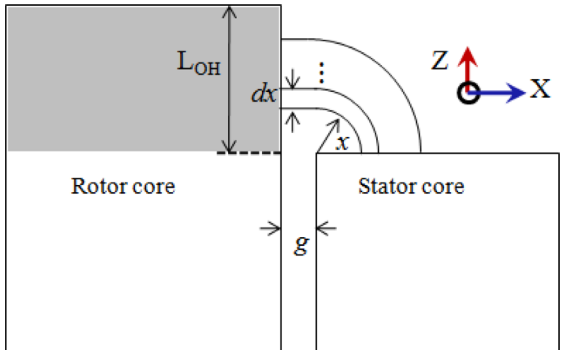

Fig. 5. (Color online) Simplified permeance model of linkage flux in Part II.

$$P_{g,PartII}(\alpha) = \int_{g}^{L_{OH}} \frac{\mu_0(\alpha_p 2\pi r/P)}{g+\frac{\pi}{2}x}dx = \frac{2\mu_0(\alpha_p 2\pi r/P)}{\pi}\ln\left(\frac{1+\frac{\pi L_{OH}}{2g}}{1+\frac{\pi}{2}}\right). \quad (19)$$

By using reciprocal relationship between reluctance and permeance, the air-gap reluctance, $R_{g,PartII}$ is given by

$$R_{g,PartII} = P_{g,PartII}^{-1} \, . \quad (20)$$

In Part II, unlike SPM motor, the leakage flux of PM, magnet end-leakage fluxes and the leakage flux through the bridge are restricted as before because the PMs are inserted in the rotor core as shown in Fig. 6. Therefore, the corresponding reluctances and the leakage flux in Part II can be easily expressed by replacing L_{stk} with L_{OH}.

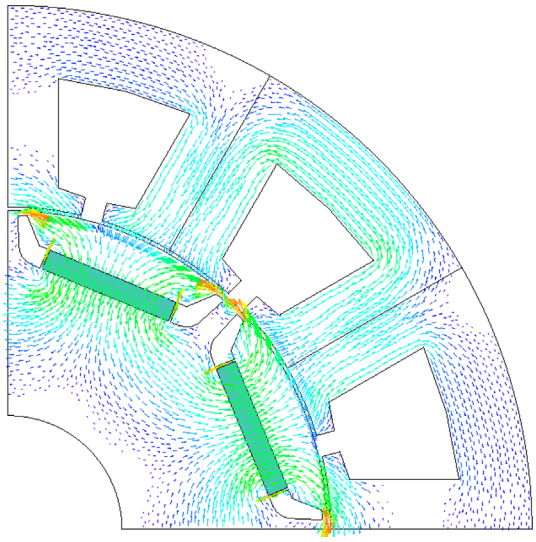

Fig. 6. (Color online) Top view: Vector plot of magnetic flux density using 3-D FEA.

$$R_{ml,PartII} = \frac{h_M}{\mu_0 L_{OH}(h_1 + h_2)/2} \tag{21}$$

$$R_{mo,PartII} = \frac{h_M}{\mu_0 \mu_r w_M L_{OH}} \tag{22}$$

$$\varphi_{mb} \approx B_{sat} A_b = B_{sat} b L_{OH} \tag{23}$$

Substituting (20), (21), (22), and (23) into (7), the air-gap flux of Part II, ϕ_{g_PartII} and total magnetic flux can be estimated for analyzing the overhang effect.

3.3. Calculation of Torque

Overall torque of IPM motor is sum of magnet and reluctance components as follows:

$$\begin{aligned} T &= \frac{3}{2}\frac{p}{2}\left[\frac{E_1}{\omega_e} i_q + (L_d - L_q) i_d i_q\right] \\ &= T_M + T_R \end{aligned} \tag{24}$$

where E_1 is fundamental amplitude of back-EMF, ω_e is electrical angular speed [rad/s], i_d and i_q are d-, and q axis current. L_d and L_q are d-, and q-axis inductances respectively.

T_M refers to the magnet torque which is the same as SPM, and T_R denotes the reluctance toque generated by the difference between L_d and L_q in (23).

The relationship between the current and flux linkage can be drawn by vector diagram as shown in Fig. 7 where ψ_f is the flux linkage generated by permanent magnet in no-load condition, ψ_o is the flux linkage generated by

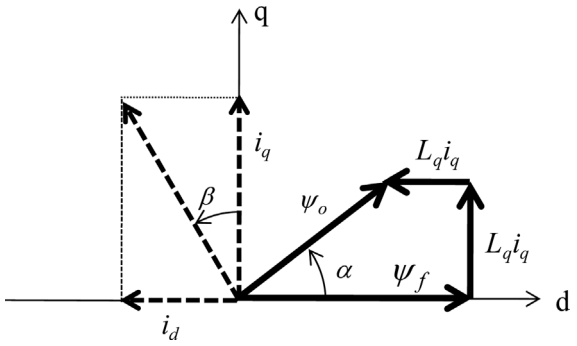

Fig. 7. Vector diagram of IPM.

permanent magnet and excited armature current, the α is the phase shift between ψ_f and ψ_o, and β is current angle. Using the vector diagram of Fig. 7, d-, and q-axis inductance can be obtained as follow:

$$L_d = \frac{\psi_o \cos\alpha - \psi_f}{i_d}, \quad L_q = \frac{\psi_o \sin\alpha}{i_q} \tag{25}$$

Since the phase shift, α can be only calculated by FEA, (25) is for FEA. In order to estimate the two inductances by lumped parameters, the inductances are divided into two parts:

$$L_d = L_{d,PartI} + L_{d,PartII}, \quad L_q = L_{q,PartI} + L_{q,PartII}. \tag{26}$$

Thus, the difference between the d-and q-axis inductances is given by

$$L_d - L_q = (L_{d,PartI} - L_{q,PartI}) + (L_{d,PartII} - L_{q,PartII}). \tag{27}$$

Assuming $L_{q,PartII} << L_{q,PartI}$ and $L_{d,PartII} << L_{d,PartI}$, due to absence of the stator core and $L_{OH} << L_{stk}$, the difference between the d-, and q-axis inductances belong to Part II is much smaller and can be disregarded. Hence, (26) is simply reduced into

$$L_d - L_q \cong (L_{d,PartI} - L_{q,PartI}). \tag{28}$$

Therefore, the reluctance torque of IPM can be calculated by inductances in Part I and is given by

$$T_R \cong \frac{3}{2}\frac{p}{2}(L_{d,PartI} - L_{q,PartI}). \tag{29}$$

The modeling of the d-and q-axis inductance by lumped parameter is well known and the conventional method is adopted as in [11]:

Regarding prediction of the back-EMF considering overhang effect, (17) and (18) are used for calculation of E_1 in (24). Finally, overall torque under load condition can be obtained by (24) and (29) without using FEA.

4. Simulation Results and Discussion

Figure 8 shows comparison results of air-gap flux density waveform of analysis models by the proposed LMCM and 2-D FEA. It is noticed that the flux density of the LMCM agrees well with the results of the FEA, which means that the modeling of the magnetic saturation and leakage flux in Part I are well considered. The little discrepancy between 2-D FEA and LMCM in Fig. 8 comes from the nonlinearity in the stator' teeth.

The back-EMF waveform by LMCM, conventional method based on teeth flux approach, and 2-D FEA are compared as shown in Fig. 9. The peak value of back-EMF by LMCM is closed to that by FEA whereas the value by conventional method is much lower.

In order to investigate the overhang effect on the back-EMF, five types of overhang ratio (OH) are selected and the comparison results are shown in Fig. 10. It can be seen that the difference between calculated value using the analytic method and FEA is increased as the OH is increased. The maximum error between the results is less than 6.5 % when OH is 30 %. Since OH over 30 % is unusual in practical motor, it is reasonable that the proposed method is effective.

Figure 11 shows good agreements of torque versus current characteristics by LMCM and FEA when β is fixed as 0°. It can be seen that remarkable discrepancy by magnetic saturation between analytic and FEA is found at over 40 A. The segregated by LMCM considering overhang effect by (24) and (29) are shown in Fig. 12. The maximum value of T_M is found when β is 0° whilst the T_R can be the max at 45°. By adding the two segregated torque components, the total toque according to current angle can be completed. The comparison results are shown in Fig. 13. In the case of OH 0%, the

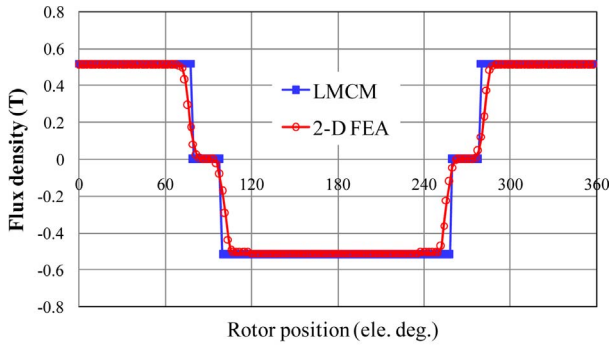

(a) non slotted air-gap flux density

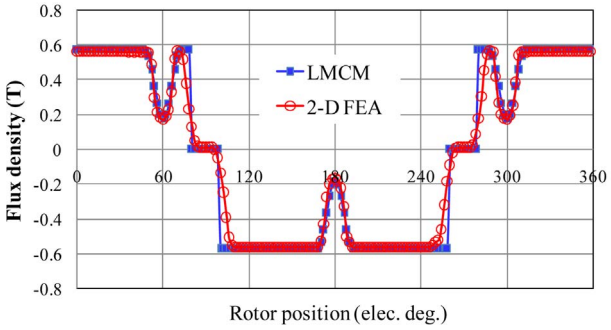

(b) slotted air-gap flux density

Fig. 8. (Color online) Comparison results of air-gap flux density.

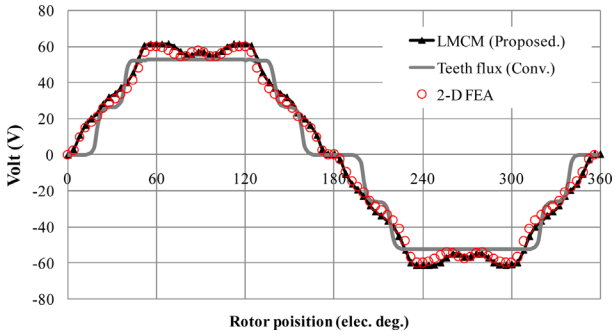

Fig. 9. (Color online) Comparison results of back-EMF at 1000 r/min.

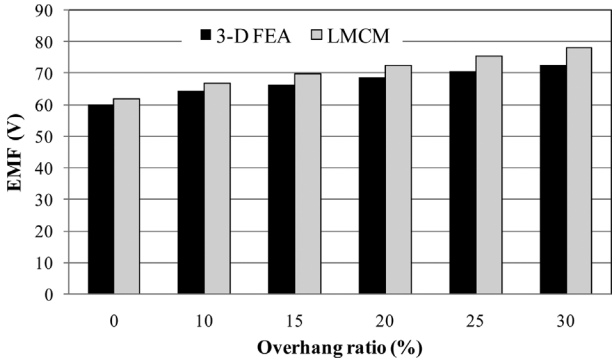

Fig. 10. Comparison of fundamental amplitude of back-EMF with respect to overhang ratio.

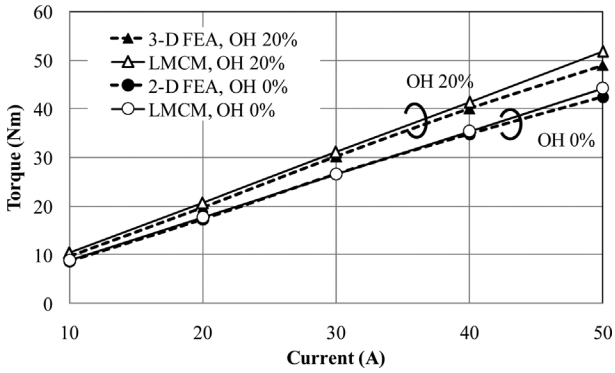

Fig. 11. Comparison of torque versus current characteristics (β = 0°).

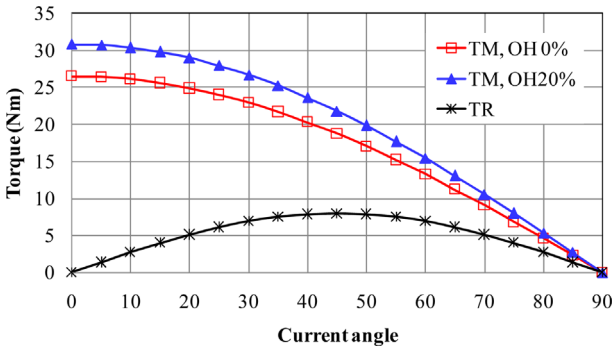

Fig. 12. (Color online) Torque segregation by LMCM. TM : magnet torque, TR : reluctance torque.

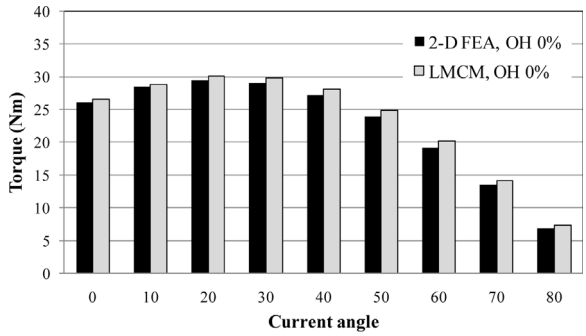

(a) OH 0%

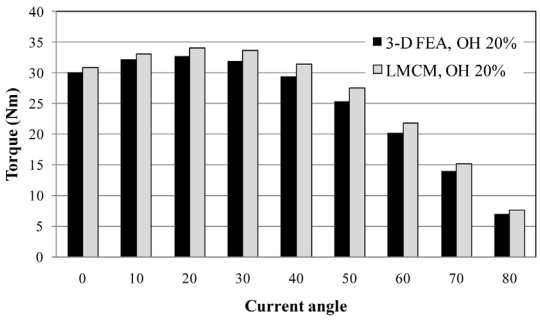

(b) OH 20%

Fig. 13. Comparison of torque with respect to current angle at rated condition.

error is less than 5 % which means that the modeling of T_M and T_R is reasonable. The maximum torque can be found at 20°. However, in the case of OH 20 %, the discrepancy becomes lager and the maximum error is about 8 % with the maximum current angle of 80°. It is interesting that the results of 3-D FEA are still smaller than that of the LMCM although additional reluctance torque by overhang effect is neglected as (28). In Fig. 13 (b), the minimum error is found when β is 0°, which means that the modeling of T_M is acceptable and T_R becomes smaller than what we expected.

In order to investigate the difference between two inductances, which is proportional to T_R, 3-D and 2-D

Table 2. Calculated difference of D-and Q axis inductances.

	Ld-Lq (mH)	Error (%)
2-D FEA, (OH 0 %)	-2.85	3.4
3-D FEA, (OH 20 %)	-2.67	9.6
Lumped parameter	-2.95	-

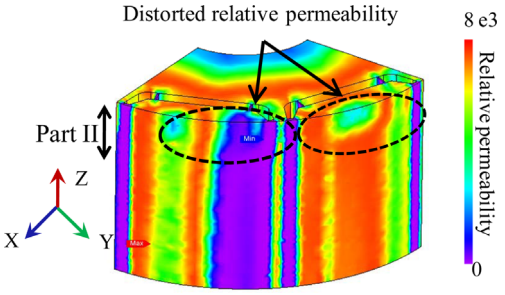

Fig. 14. (Color online) Distribution of relative permeability (OH 20 %, β = 80°).

FEA with (25) are performed and compared with the proposed method. From Table 2, it is revealed that (L_d-L_q) becomes smaller when the rotor structure has the overhang whilst a small error can be found at OH 0 %. Figure 14 shows the distribution of relative permeability of overhang rotor structure when β is fixed as 80°. It can be seen that the relative permeability indicating saturation level is not axially uniform especially at Part II. Thus, we can say that the reason why the reluctance torque becomes smaller is on the distortion distribution of relative permeability in the overhang region. Thus, from Fig. 13, it can be seen that IPM with the overhang is useful for low speed applications because it has high magnet torque whilst the reluctance component becomes lower.

Although the discrepancy between results of 3-D FEA and the LMCM do exist, the proposed method is still useful because it can estimate the back-EMF, maximum torque with low error.

5. Conclusion

In this paper, the overhang effect on the performance of IPM motor using a LMCM is investigated. Under an assumption that the separated regions indicating the overhang and non-overhang parts do not affect each other, the increase of air-gap flux and back-EMF are calculated. It is confirmed that the discrepancy of simulation results for back-EMF between 3-D FEA and the proposed method is available.

In addition, a study considering the load condition according to current angle is presented. From the comparison results, it is worthy to be noted that the overhang

affect the saturation level in the rotor core and thus resulting in decrease of reluctance torque which is supposed to be constant. As a results, the calculated torque by LMCM is little higher than that of 3-D FEA.

From the simulation results, the proposed method can be effective in terms of determining the overhang length considering machine's performance with a short time.

Acknowledgements

This research was supported by Kyungpook National University Research Seed Fund, 2014.

References

[1] K. C. Kim and J. Lee, IEEE Trans. Magn. **41**, 10 (2005).
[2] K. C. Kim, D. H. Koo, and J. Lee, IEEE Trans. Magn. **43**, 4 (2006).
[3] J. M. Seo, I. S. Jung, H. K. Jung, and J. S. Ro, IEEE Trans. Magn. **50**, 5 (2014).
[4] K. Y. Hwang, H. Lin, S. H. Rhyu, and B. I. Kwon, IEEE Trans. Magn. **48**, 5 (2012).
[5] J. P. Wang, D. K. Lieu, W. L. Lorimer, and A. Hartman, J. Appl. Phys. **83**, 11 (1998).
[6] Liang Fang, Do-Jin Kim, and Jung-Pyo Hong, Journal of KIEE, **60**, 759 (2011).
[7] L. Zhu, S. Z. Jiang, Z. Q. Zhu, and C. C. Chan, IEEE Trans. Magn. **45**, 8 (2009).
[8] J. H. Seo and H. S. Choi, IEEE Trans. Magn. **50**, 10 (2014).
[9] J. H. Seo and H. S. Choi, IEEE Trans. Appl. Supercond. **24**, 3 (2014).
[10] J. H. Seo, J. Magn. **18**, 3 (2013).
[11] J. R. Hendershot and T. J. E. Miller, Design of brushless permanent-magnet machines (2010).
[12] Z. Q. Zhu and D. Howe, IEEE Trans. Magn. **29**, 1 (1993).
[13] D. Zarko, D. Ban, and T. A. Lipo, IEEE Trans. Magn. **42**, 7 (2006).
[14] Z. Q. Zhu, L. J. Wu, and Z. P. Xia, IEEE Trans. Magn. **46**, 4 (2010).